Desalination and Water Treatment
www.deswater.com

doi:10.5004/dwt.2018.22607

116 (2018) 267–276
June

Thermal oxidation etching process of g-C_3N_4nanosheets from their bulk materials and its photocatalytic activity under solar light irradiation

Faisal Al Marzouqi[a], Rengaraj Selvaraj[a,*], Younghun Kim[b*]

[a]*Department of Chemistry, College of Science, Sultan Qaboos University, P.O. Box 36, P.C. 123, Al-Khoudh, Muscat, Oman, Tel. 00968-2414-2436, email: srengaraj1971@yahoo.com (R. Selvaraj)*
[b]*Department of Chemical Engineering, Kwangwoon University, Seoul 139-701, Korea, Tel. +82-2-940-5769, email: korea1@kw.ac.kr (Y. Kim)*

Received 17 May 2018; Accepted 6 June 2018

ABSTRACT

The behaviour of g-C_3N_4 samples under thermal oxidation etching process were investigated. The g-C_3N_4 samples were prepared from melamine powder by following a two-step heating method in a semi-closed system. The effects of different thermal oxidation etching processes were systematically investigated to understand the influence of this process on the g-C_3N_4 properties. The transformation of g-C_3N_4 3 h (bulk) to g-C_3N_4 12 h (nanosheets) was confirmed by conducting systematic studies including scanning electron microscopy (SEM), energy-dispersive X-ray spectroscopy (EDX), X-ray diffraction (XRD), X-ray photoelectron spectroscopy (XPS), Photoluminescence (PL), Fourier-transform infrared spectroscopy (FTIR), UV-vis diffuse reflectance spectroscopy (UV-vis DRS), Brunauer Emmett Teller (BET) analysis and particle size analysis. Methylene blue (MB) dye was selected as a model organic pollutant to evaluate the photocatalytic activity of the g-C_3N_4 samples. The XPS, UV-vis DRS and FTIR results indicated no major effect of the oxidation etching process on bulk g-C_3N_4 in the first 9 h. However, some variations were observed in XRD, particle size and BET analysis indexing where the etching process was observed to reduce the particles size and lower the number of layers on the g-C_3N_4 backbone. After 12 h of oxidation etching treatment, XPS and FTIR spectra showed some variation in the C-H, CO and N pyridinic structure of g-C_3N_4. MB results showed faster (150 min) degradation by the g-C_3N_4 nanosheets compared to bulk g-C_3N_4 (240 min) under solar irradiation. This can be attributed to other factors such as smaller particle size, rich carbon surface and high surface area exhibited by the g-C_3N_4 nanosheets. Thermal oxidation etching of g-C_3N_4 for 12 h is more effective at enhancing the photocatalytic degradation of organic pollutants under solar irradiation.

Keywords: Carbon nitride; Dyes; Melamine; Nanosheets; Photocatalysis; Solar light

1. Introduction

Photocatalytic semiconductors are promising materials for addressing global environmental and energy challenges. Highly active photocatalysts that can degrade environmental pollutants or can split water under solar light irradiation have potential applications in environmental decontamination and solar energy conversion. The semiconductor photocatalysts that have been developed to date include transition metal oxides, metal sulphides and oxy-nitrides [1–3]. Recently, interest has shifted to producing narrow band gap semiconductors opposed to the commonly used wide band gap photocatalyst such as TiO_2 and ZnO [4,5]. Some of the traditional semiconductor-based photocatalysts have several limitations that include (i) weak light absorption, (ii) non-suitable redox potential for the photocatalytic reaction, (iii) short-term stability, and/or (iv) high material costs [6–9].

Wang et al., recently reported on graphite-like carbon nitride (g-C_3N_4), which is an active semiconductor that can be used for water splitting under visible light irradiation [10]. The g-C_3N_4 is a polymeric semiconductor that

*Corresponding author.

can exist in 3D (bulk) and 2D (nanosheet) structures, and has a band gap of 2.7 eV [11,12]. This organic semiconductor has attracted attention around the world due to its suitable redox potential, low band gap, greater thermal-chemical stability and suitability for large-scale production from low-cost precursors such as urea, thiourea, melamine, cyanamide and dicyanadiamide [12–15]. Moreover, its preparation is comparatively simple. g-C_3N_4 bulk materials can be synthesized via thermal polycondensation of conjoint monomers to obtain a typical mass polymer in a low vacuum system or under a high pressure [16–18]. Several research groups have reported use of a semi-closed system to obtain g-C_3N_4 under ambient pressure, which, from an industrial point of view, is more convenient to produce this material at a large scale [19,20]. In addition, g-C_3N_4 nanosheets have been obtained from g-C_3N_4 bulk materials using methods such as acidification, sonication and thermal oxidation processes [21,22]. However, the duration of oxidation processes varied among research groups, leaving a big debate regarding the effect of this process on g-C_3N_4 properties. To the best of our knowledge no systematic investigation has been done on the effect of the duration of thermal oxidation etching process on the formation of g-C_3N_4 nanosheets from g-C_3N_4 bulk materials. In this study, we investigate the effect of two-step heating method on the nature of the g-C_3N_4 in a semi-closed system under ambient pressure. After obtaining,the bulk g-C_3N_4 material a second step called thermal oxidation etching process was carried out for different time durations started from 3 h up to 12 h in steps of 3 h at 550°C without nitrogen. The effect of the second step on g-C_3N_4 bulk was investigated via various techniques along with the photocatalytic activity evaluation of the as-prepared g-C_3N_4 samples using methylene blue dye solution (5 mg/L) as a model organic pollutant. The results showed that g-C_3N_4 nanosheets were obtained after heating the melamine powder at 550°C for 12 h. In the first 9 h of treatment, no major changes were observed regarding the g-C_3N_4 structure. Oxygen acted as an etching agent on the g-C_3N_4 surface and reduced the number of layers making the material fluffier. After 12 h of etching, the oxygen and H_2O intercalate in between layers, allowing the oxidation etching process to occur more, resulting in surface modification with groups such as CO, C-H and N pyridinic.

2. Experimental

2.1. Materials and methods

Melamine powder was purchased from Sigma-Aldrich (M2659 ALDRICH) and was used without further purification. The synthesis of the g-C_3N_4 photocatalyst was performed in a muffle furnace by directly heating melamine in a semi-closed system. One gram of melamine powder was placed into an alumina crucible and covered with a lid. Thereafter, direct heating was applied by increasing the temperature to 550°C at a heating rate of 20°C/min under a nitrogen flow for 25 min. Thermal oxidation and etching was further performed at 550°C without nitrogen for 3–12 h in steps of 3 h. After cooling, the product was collected for further analysis.

2.2. Characterization

The crystal phases of the samples were observed by X-ray diffraction (XRD) analysis using a MiniFlex600 bench top X-ray diffractometer with graphite monochromatized Cu Kα radiation (λ = 1.540 Å) source. The morphology of the samples was examined using a field emission scanning electron microscope (FESEM, JSM-7800F JOEL, Japan). A maximum working voltage of 30 kV, maximum resolution of 0.8 nm, and a working distance of 10 mm was used during measurements. X-ray photoelectron spectroscopy (XPS) was carried out using a multi-probe X-ray photoelectron spectroscope (XPS) (Omicron Nanotechnology, Germany). The XPS spectra were divided to individual components using the Casa XPS software (Casa Software Ltd). During measurement, the sample surface was flooded with electrons using a built in neutralizer. UV-vis diffuse reflection spectroscopic (UV-vis DRS) measurements were conducted using the Perkin Elmer Lambda 650S spectrometer. Infrared spectra were obtained on a CARY 600 FTIR from Agilent Technologies. Brunauer Emmett Teller (BET) surface area analysis was carried out using ASAP2010 under liquid N_2 with 50 P/P_o points, Micromeritics, USA. The particle sizes were measured using Microtrac particle sizer machine. Photoluminescence (PL) behaviour was measured using a Perkin-Elmer LS 55 luminescence spectrometer.

2.3. Photocatalytic activity test

Methylene Blue (MB) dye was chosen as a model of an organic degrading pollutant to test the photocatalytic activity of the as-prepared g-C_3N_4 samples. All photodegradation reaction experiments were carried out in a photocatalytic reactor batch system consisting of a cylindrical borosilicate glass reactor vessel with an effective volume of 500 mL. The studies were conducted in March, when the solar light intensity varied from 1300 to 1400 W/m^2 and the temperature varied from 25 to 29°C during the measurements. The experiment carried out in the open atmosphere with an air diffuser fixed at the reactor to uniformly disperse oxygen into the solution. The reaction suspensions were prepared by adding 0.1 g of as-prepared g-C_3N_4 sample into 250 ml of aqueous methylene blue solution (0.4 mg/ml), with an initial concentration of 5 mg/L. Prior to illumination, the reaction suspensions were magnetically stirred for 30 min in the dark to ensure adsorption-desorption equilibrium between the photocatalyst and methylene blue. Upon illumination, 6 ml aliquots of suspension were taken from the reactor at scheduled time intervals. The sample was centrifuged at 8000 rpm for 5 min and then filtered to remove the catalyst. The filtrate was analysed on the UV-Vis spectrophotometer to evaluate the degradation of the MB dye.

3. Results and discussion

3.1. Characterization of g-C_3N_4 nanosheets

Thermal oxidation etching was employed to synthesise metal-free g-C_3N_4 nanosheets. First, the g-C_3N_4 bulk material was obtained by subjecting melamine to polycondensation under a nitrogen flow at 550°C at a heating rate of 20°C /min for 25 min. Then, further treatment was performed

without nitrogen for 3, 6, 9 and 12 h. The different amounts of g-C_3N_4 powder obtained at these different treatment durations are shown in Fig. 1a. The yield of g-C_3N_4 powder increased with reaction time from 3 to 12 h. This variation in yield indicates modification in the sample density as a result of oxidation etching process. The schematic representation of the oxidation etching process mechanism is shown in Fig. 1b.

Fig. 2 show SEM images of g-C_3N_4 samples prepared with different durations of thermal oxidation etching. The SEM images show sheet-like microstructures. However, the g-C_3N_4 sheets obtained after 12 h seems to be softer and fluffier (Fig. 2d inset) compared to the samples treated for 3, 6 and 9 h, which seems to be more solid (Figs. 2a, 2b, 2c). Micrometre-sized sheets were obtained due to aggregation of different nanometre-sized crystal stacking layers [23–25]. The elemental composition of the prepared samples was identified using energy dispersive X-ray spectroscopy (Fig. 2e). The EDX analysis shows main signals from carbon (C) and nitrogen (N). The other signals (Al) are from the sample holder and the platinum used for sample coating. No other peaks were detected, confirming the high purity of the as obtained products.

Fig. 3 shows the XRD patterns of the g-C_3N_4 prepared via thermal oxidation for 3, 6, 9 and 12 h. All samples exhibited two diffraction peaks. The first peak at around 27.90° corresponds to the (002) peak that is characteristic of interlayer stacking of aromatic systems, and the second diffraction peak at around 13.05° is indexed to the (100) peak that represents inter-planar separation. These diffraction peaks are in good agreement with those reported for g-C_3N_4 and were retained during thermal oxidation [26], indicating the existence of the graphite-like structure of g-C_3N_4. The crystallite grain size for the samples were calculated using the Scherre's equation $D = K\lambda/(\beta\cos\theta)$ where K is the shape factor (1), θ is the Bragg's diffraction angle, λ is the wavelength of X-ray diffractometer used in the analysis (λ = 1.540 Å) and β is the full width at half maximum (FWHM) of the respective XRD sample peak. The grain sizes were found to be 42, 43, 44 and 52 nm for the samples prepared at 3, 6, 9 and 12 h, respectively. This kind of increasing in the grain size value is expected and it has been observed previously [27]. It can be attributed to the further 2D growth happening during the formation of g-C_3N_4 nanosheets due to longer reaction time. Moreover, the overall intensity of the diffraction peaks decreased as the duration of the thermal oxidation increased up to 12 h, and this is attributed to the reduction in the structural correlation length due to a decrease in the number of layers, reflecting the formation of g-C_3N_4 nanosheets.

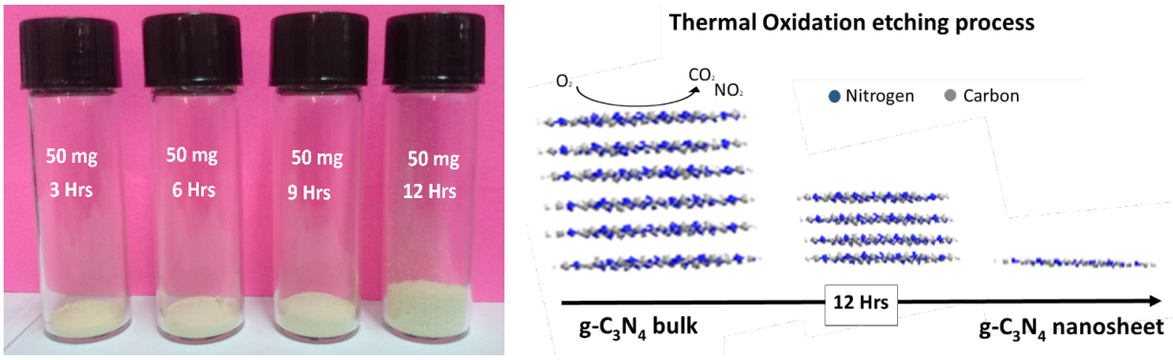

(a) (b)

Fig. 1. (a) The volume of 50 mg of g-C_3N_4 powder heated at 550°C for different durations of thermal oxidation (b) Schematic illustration of the preparation of the g-C_3N_4 nanosheet.

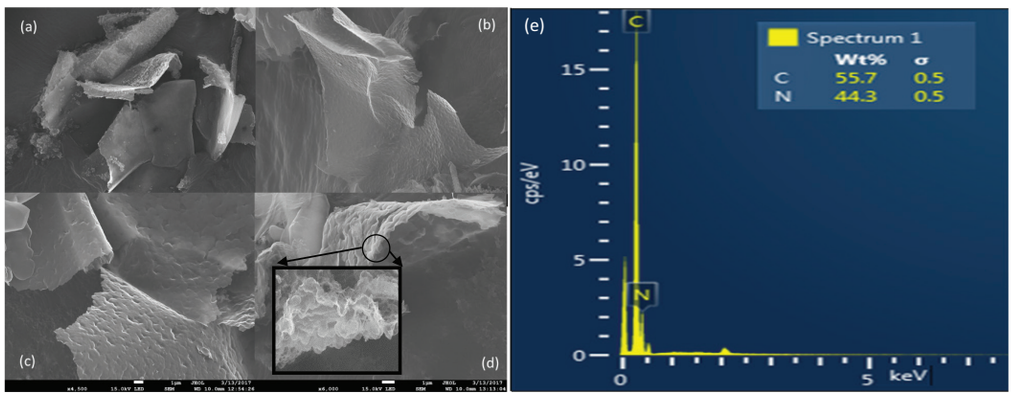

Fig. 2. SEM images of g-C_3N_4 prepared using thermal oxidation etching with different durations. (a) 3 h, (b) 6 h, (c) 9 h, and (d) 12 h.

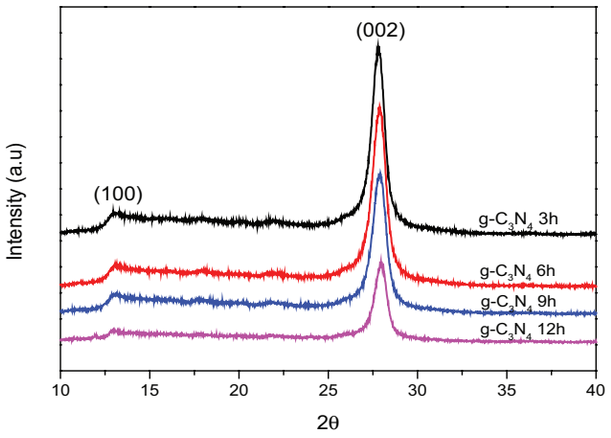

Fig. 3. XRD patterns of g-C_3N_4 samples obtained by heating melamine and conducting thermal oxidation for various times of 3, 6, 9 and 12 h.

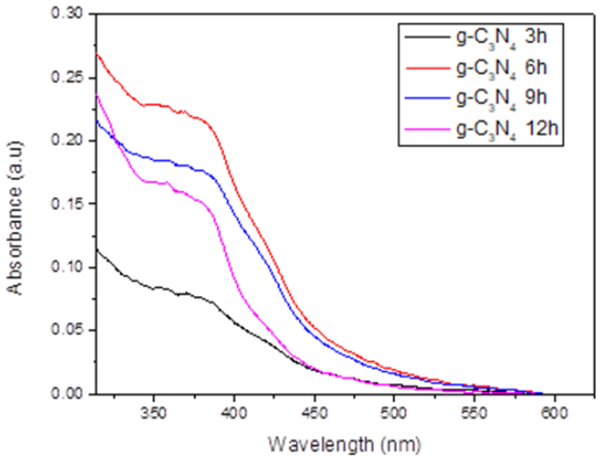

Fig. 4. UV-Vis absorption spectra for g-C_3N_4 samples obtained at various thermal oxidation time.

3.2. Optical properties of nanosheets

The optical properties of the various g-C_3N_4 samples were determined by UV-Vis diffuse reflectance spectroscopy (UV-vis DRS), and the results are shown in Fig. 4. The band edge shifted to a longer wavelength from 390 nm for g-C_3N_4 heated for 3 h to up to 410 nm for the rest of the samples treated for longer times, which is consistent with previous results [28,29]. However, the samples absorbed near UV and visible light up to 470 nm. The spectra also show a long absorption tail for the samples treated for longer time, which can be attributed to structural defects that formed with longer treatment. The optical band gap was calculated using the Tauc plot (the curve of $(E*A)^2$ versus E where E is the energy in eV and A is the absorption) [30]. The band gap values for the g-C_3N_4 samples obtained at various thermal oxidation times were calculated to be 2.7, 2.65, 2.7 and 2.7 eV, respectively (Fig. 5). Interestingly it seemed the thermal oxidation etching process had no effect on band gap energies confirming that there were no major changes on the g-C_3N_4 main structure in all samples.

The Fourier transform infrared (FTIR) spectra of the samples are shown in Fig. 6. The results further confirm the presence of the graphite like structure of carbon nitride. The broad peak in the range of 3000–3500 cm^{-1} is due to NH stretching modes and water absorbed on the surface. The bands at 1200–1600 cm^{-1} are characteristic of the typical stretching vibrations of CN heterocycles. In addition, the s-triazine ring vibrational mode was observed at 801 cm^{-1}, which is in good agreement with the previously reported results and confirms the formation of g-C_3N_4 [31,32]. There were no major differences in the FTIR spectra of all the samples. However, there was some broadening in the peak at 3000–3500 cm^{-1}, which is indexed to CO vibration.

XPS measurements performed to determine the chemical composition of different g-C_3N_4 samples (Fig. 7a) and to follow the core levels changes of the constituent elements (Figs. 7b, 8a and 8b) as a results of increasing the thermal oxidation time. The XPS survey spectra shows that the main elements present were carbon (C1s), nitrogen (N1s) and low concentration of oxygen (O1s). The XPS spectra were analysed and divided into high-resolution individual components using Casa XPS software. The amount of each element and the carbon to nitrogen ratio (C/N) (wt%) are shown in Table 1. There was a slight increase in the C/N ratio with increase in treatment time. This enhancement may indicate a carbon-rich surface which may enhance the photocatalytic activity by promoting charge carrier separation [33]. In addition, the carbon to nitrogen ratio remain close to the C_3N_4 formula by a variation of 0.15 to 0.29 wt%, which is acceptable taking the inconsideration the sample surface defects. Fig. 7b represents the O 1s where the main peak was observed at 531.6 eV. Interestingly, the oxygen band structure remained unchanged after heating the samples for 12 h indicating that oxygen is not involved in the g-C_3N_4 backbone structure and it has been used only as etching agent during the oxidation etching process and the modification of the surface structure. Therefore, the amount of oxygen slightly increased from 0.65 wt% for g-C_3N_4 heated for 3h up to 0.78 wt% for g-C_3N_4 treated for 12 h. In general, the binding energies for carbon nitride materials are mainly located in the range between 400 and 398 eV for the main nitrogen (N1s) peak and between 286 to 289 eV for the main carbon (C1s) peak [34]. The carbon and nitrogen core levels are shown in Figs. 8a and 8b where the binding energies at 286.7, 288.4 and 289.2 eV are indexed to carbon from C-NH_2, C-N and C=N respectively while, the binding energies at 397.1, 397.1 and 400.3 eV are ascribed to nitrogen from C=N- C, N-$(C)_3$ and C-N-H respectively. The investigation revealed that no changes occurred for carbon and nitrogen core levels for samples treated up to 9 h. However, after treating the sample for 12 h, low intensity core levels peaks started appearing indicating surface modification. In the case of carbon, two peaks appeared at binding energies 284.27 and 290.2 eV. The peak at 284.27 eV could be attributed to C-C or C-H carbons while the other peak at 290.2 eV can be assigned to CO resulting from etching process and adsorbed on the sample surface [35,36]. In the case of nitrogen, the peak at binding energy 393.6 eV can be assigned to edge type N pyridinic. This N pyridinic peak has been reported and was observed for the sample treated for 12 h because higher energy or long treatment time is required for such structures [37–39]. The

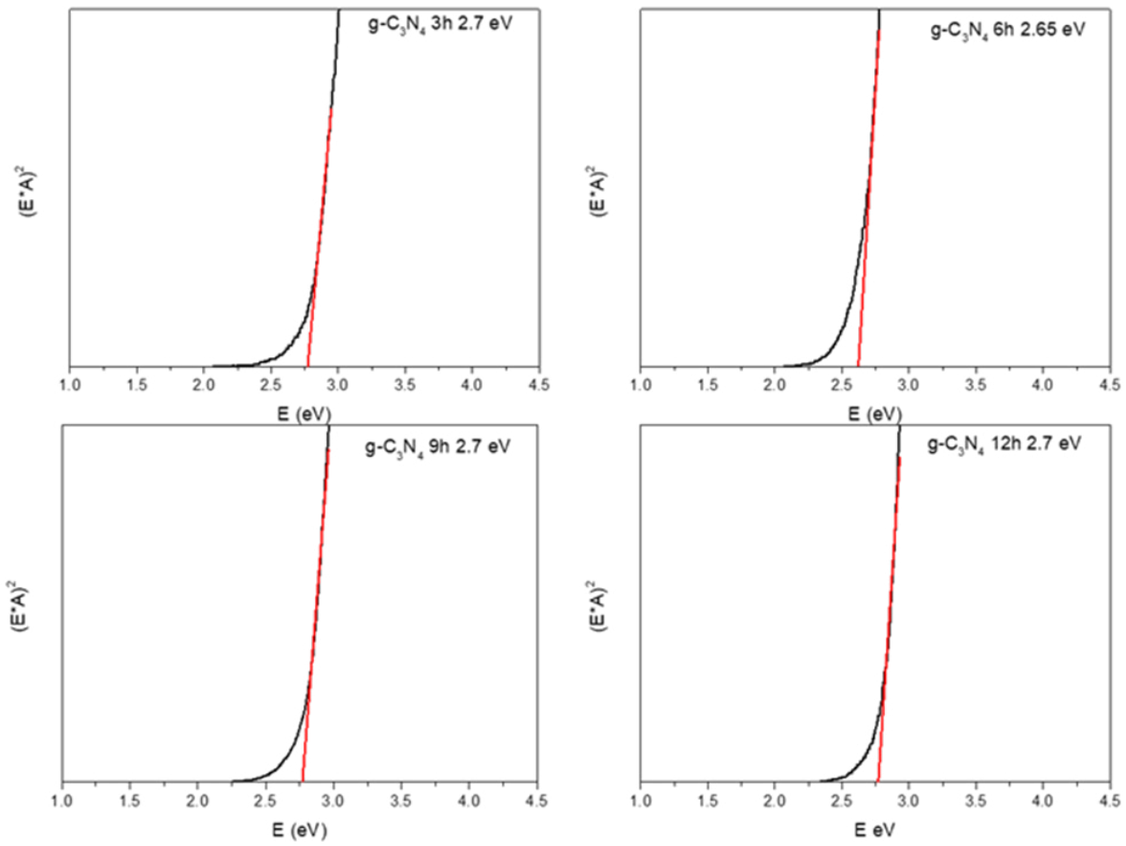

Fig. 5. Tauc plots with estimated band gap value for g-C_3N_4 samples obtained at various thermal oxidation.

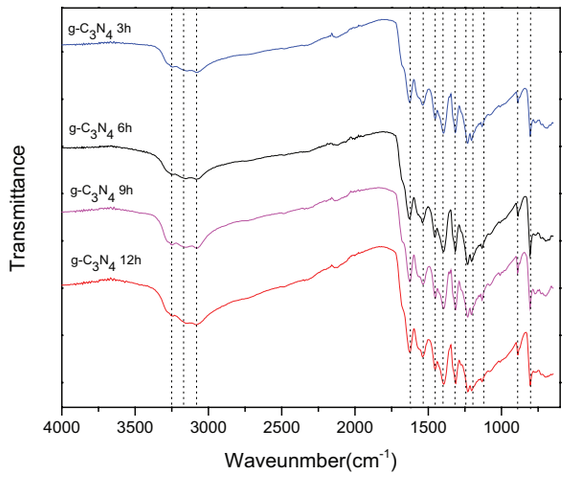

Fig. 6. FTIR spectra for g-C_3N_4 samples obtained at various thermal oxidation time.

appearance of CO in the XPS after treating the sample for 12 h can be explained by the oxidation etching process that occurred on the surface of the sample.

Fig. 9 shows the photoluminescence emission spectra with an excitation wavelength of 360 nm for the g-C_3N_4 samples at room temperature. For all samples, the main emission peak is centred at about 450 nm and can be attributed to recombination of the photo-generated electron-hole pairs in the g-C_3N_4. A higher emission intensity indicates an increase in the recombination rate of the photo-generated electron-hole pairs, and the results indicate that the g-C_3N_4 heated for 12 h has the highest formation of photo-generated electron-hole pairs and recombination rate while the g-C_3N_4 heated for 3 h had the lowest. This decrease in intensity can be attributed to electron trapping within the bulk of the material due to a crystal mismatch that prevents electron-hole pair recombination [40].

The nitrogen adsorption desorption isotherms analysis was performed to investigate the BET surface area and porosity of the samples. The g-C_3N_4samples showed a type 3 shape of isotherms according to the IUPAC classification (Fig. 10). This shape indicates the occurrence of slightly mesoporous-like structure. The presence of the mesopores are due to the aggregation of sheets to form the bulk g-C_3N_4, leaving pores in between [41]. The BET surface area and porosity results are showing in Table 2. The BJH Adsorption Surface Area of pores decreased with increase in the oxidation etching process time indicating the transformation of the multilayers of g-C_3N_4 3 h (bulk) to few layers of g-C_3N_4 nanosheets after 12 h. On the other hand, the g-C_3N_4 treated for 12 h showed a smaller BET surface area compared to other samples. Since the BET measurement was done for

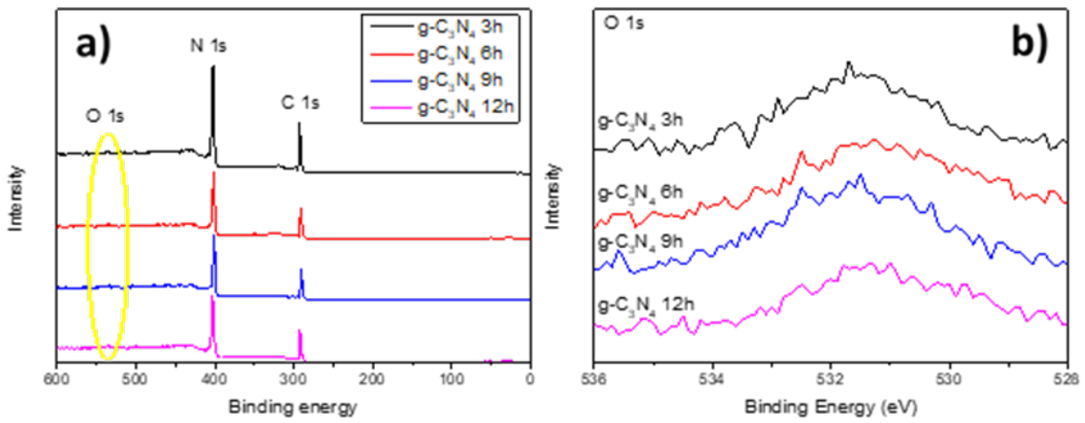

Fig. 7. (a) The XPS survey spectrum with XPS spectra of O1s (b) peak.

Table 1
The amount of C, N, and O in different g-C_3N_4 samples

XPS surface elemental analysis				
Content (%)	C	N	O	C/N
g-C_3N_4 3 h	42.23	56.92	0.65	0.74
g-C_3N_4 6 h	42.28	57.01	0.71	0.74
g-C_3N_4 9 h	44.07	55.16	0.77	0.79
g-C_3N_4 12 h	43.68	55.54	0.78	0.78

dry powder sample, this decline in the surface areas could be attributed to the significantly low amount of surface area available for nitrogen adsorption due to the overlap of the single nanosheets [42]. Particles size analysis was also investigated in order to confirm the reduction of g-C_3N_4 multilayers structure (bulk) to few layered g-C_3N_4 nanosheets with smaller size particles after heating the sample for 12 h. The particle size distribution of samples was showing in Fig. 11, where the average particle size was 4967, 4139, 2280 and 1783 nm for g-C_3N_4 3 h, g-C_3N_4 6 h, g-C_3N_4 9 h and g-C_3N_4 12 h respectively. This decline in the particle size is attributed to thermal oxidation etching process.

3.3. Evaluation of the photocatalytic activity

Methylene blue was selected as the pollutant to investigate the photocatalytic degradation of the g-C_3N_4 prepared at various thermal oxidation times under solar irradiation. Methylene blue is the most common material in studies of the performance of semiconductor photocatalytic nanomaterials using UV-Vis absorption spectra, where the maximum absorptive energy is at 664 nm [43]. The photocatalytic degradation of Methylene Blue using g-C_3N_4 prepared with different heating times is shown in Fig. 12a as a function of the degradation time. This figure indicates that compared to the g-C_3N_4 prepared at shorter treatment time, the g-C_3N_4 samples heated for 12 h have superior performance in the degradation of methylene blue and faster degradation rate. Fig. 12b shows that the band intensity at 664 nm gradually decreased with irradiation time. This is evidence of the g-C_3N_4 being more efficient in the degradation of methylene blue. The MB peak at 664 nm gradually blue shifted to shorter wavelength during degradation due to hypsochromic shift [44]. Hence, this photocatalyst has great potential for use in practical applications when compared to the other g-C_3N_4 catalysts heated for shorter time intervals.

4. Conclusion

In this work, an investigation of behaviour of g-C_3N_4 samples under thermal oxidation etching process was demonstrated. The g-C_3N_4 nanosheets were obtained after performing the etching process for 12 h. The g-C_3N_4 12 h showed higher photocatalytic activity under solar irradiation. XPS, UV-DRS and FTIR analysis showed no major changes in g-C_3N_4 in the first 9 h of treatment. However, some variation was observed in XRD, particle size and BET analysis confirming that the etching process was mainly involved in reducing the particles size and lowering the number of layers where the main structure of g-C_3N_4 remained same. After 12 h treatment some C-H, CO and N pyridinic structures were evident. MB degradation by the g-C_3N_4 nanosheets under solar irradiation was faster (150 min) than with g-C_3N_4 bulk material (240 min). This was attributed to the smaller particle size, rich carbon surface and high surface area exhibited by the g-C_3N_4 nanosheets. Therefore, heat treatment of g-C_3N_4 for 12 h is more effective and the photocatalytic degradation of organic pollutants under solar irradiation.

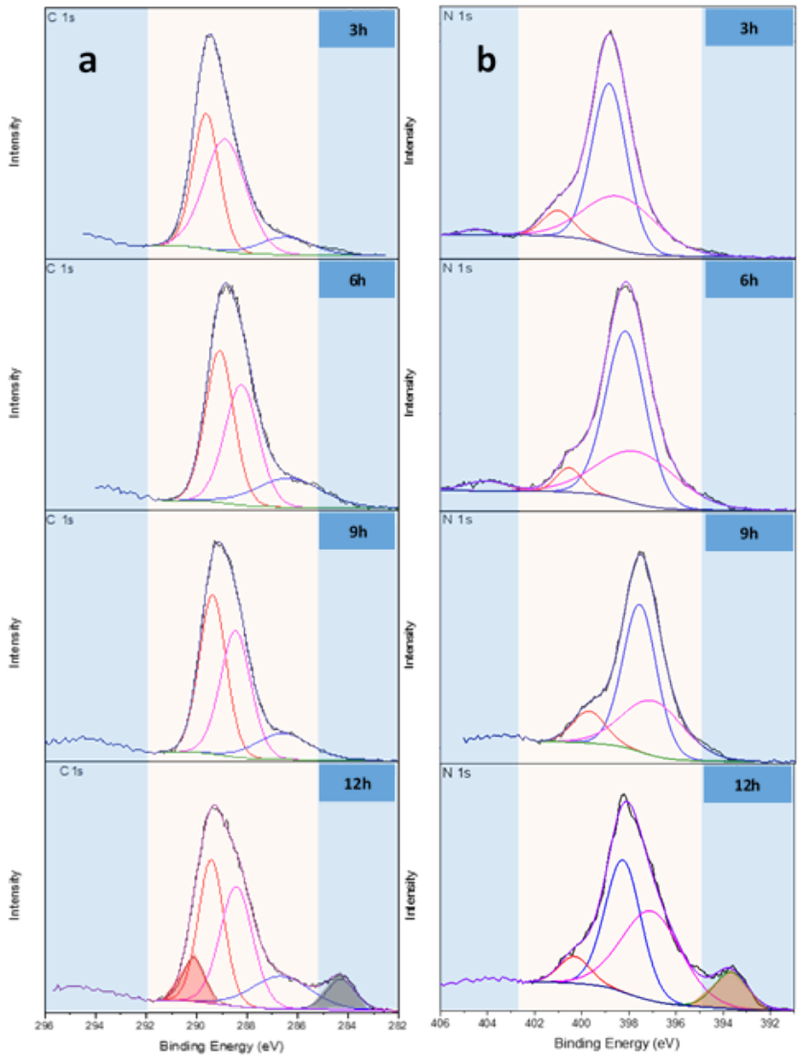

Fig. 8. (a) The XPS core levels C1s and (b) N1s of the g-C_3N_4 samples.

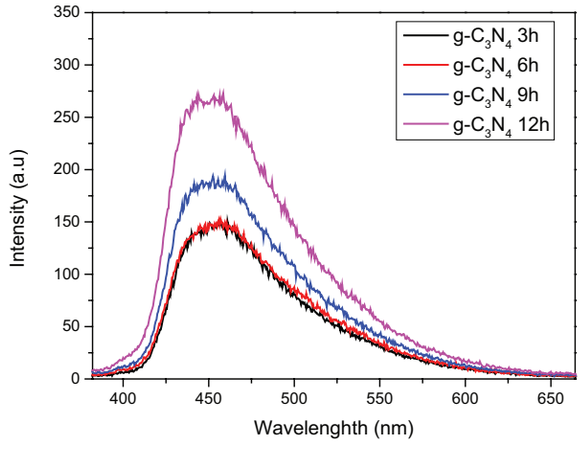

Fig. 9. Comparison of photoluminescence (PL) spectra of g-C_3N_4 prepared at different thermal oxidation time.

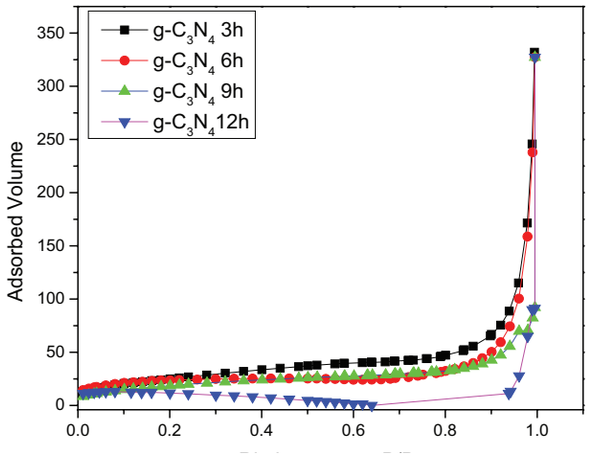

Fig. 10. BET surface area plot of g-C_3N_4 samples.

Table 2
The BET surface area and porosity results

Sample ID	BET surface area (m^2/g)	BJH adsorption surface area of pores (m^2/g)	Adsorption average pore diameter (Å)
g-C_3N_4 3 h	94.2435	123.0573	112.5594
g-C_3N_4 6 h	79.8364	107.1095	122.9991
g-C_3N_4 9 h	72.1848	96.5353	86.3756
g-C_3N_4 12 h	30.1063	37.8759	133.432

Acknowledgements

R. Selvaraj is grateful to Sultan Qaboos University for providing financial support to carry out this work under SQU-UAEU joint collaborative research Grant (CL/SQU-UAEU/16/04). Y. Kim thanks to the National Research Foundation of Korea (2017R1A2B4001829).

Conflict of interest

The authors declare no competing financial interest.

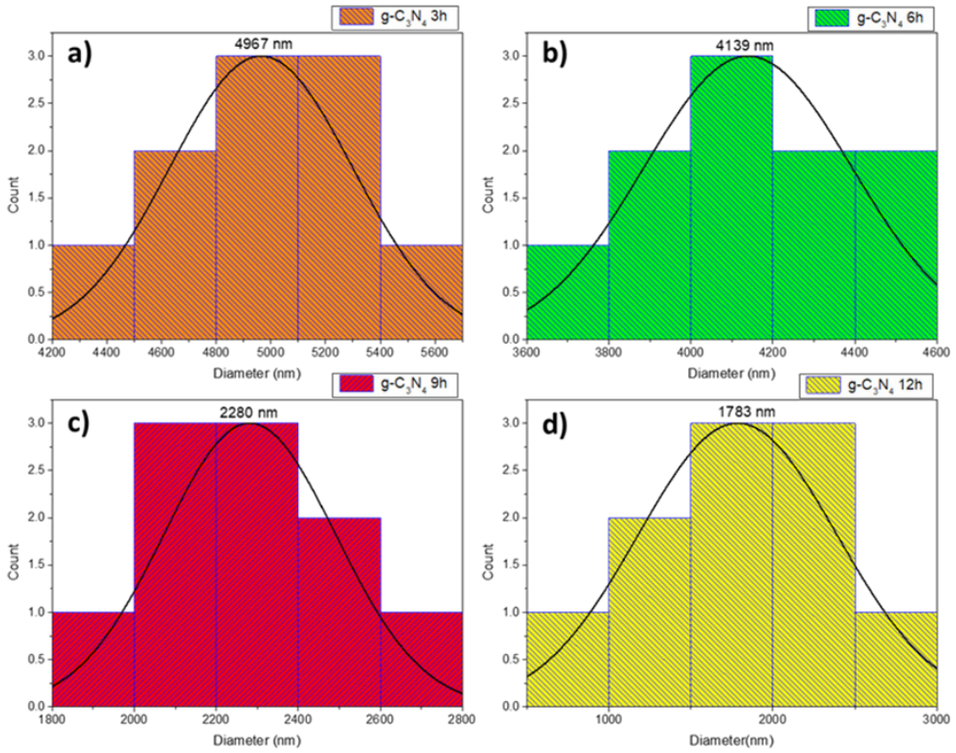

Fig. 11. Histogram of corresponding particles size distribution (a) g-C_3N_4 3 h, (b) g-C_3N_4 6 h, (c) g-C_3N_4 9 h, (d) g-C_3N_4 12 h.

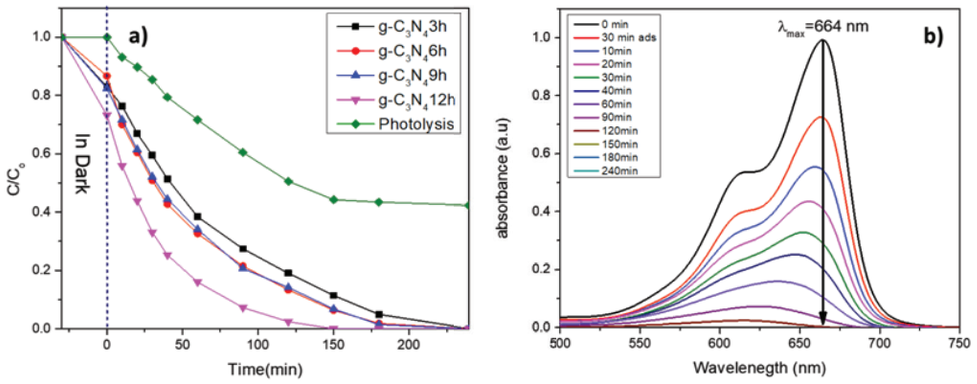

Fig. 12. (a) The photocatalytic degradation of Methylene Blue with g-C_3N_4 under solar light irradiation. (b) Time-dependent UV-vis absorption spectra of methylene blue (5 mg/L) degradation with g-C_3N_4 prepared at different thermal oxidation time under solar light irradiation [catalyst dosage 0.4 mg/ml, MB solution volume 250 ml (5 ppm), light source solar].

References

[1] F.E. Osterloh, Inorganic materials as catalysts for photochemical splitting of water, Chem. Mater., 20 (2008) 35–54.

[2] A. Nasrollahpour, S.E. Moradi, Photochemical degradation of methylene blue by metal oxide-supported activated carbon photocatalyst, Desal. Water Treat., 57(19) (2016) 8854–8862.

[3] K. Qi, S. Karthikeyan, W. Kim, F. Al Marzouqi, I.S. Al-Khusaibi, Y. Kim, R. Selvaraj, Hydrothermal synthesis of SnS_2 nanocrystals for photocatalytic degradation of 2,4,6-trichlorophenol under white LED light irradiation, Desal. Water Treat., 92 (2017) 108–115.

[4] X. Chen, S. Shen, L. Guo, S.S. Mao, Semiconductor-based photocatalytic hydrogen generation, Chem. Rev., 110 (2010) 6503–6570.

[5] A. Kudo, Y. Miseki, Heterogeneous photocatalyst materials for water splitting, Chem. Soc. Rev., 38 (2009) 253–278.

[6] X. Lang, X. Chen, J. Zhao, Heterogeneous visible light photocatalysis for selective organic transformations, Chem. Soc. Rev., 43 (2014) 473–486.

[7] Y. Bai, T. Chen, P. Wang, L. Wang, L. Ye, X. Shi, W. Bai, Size-dependent role of gold in g-C_3N_4/BiOBr/Au system for photocatalytic CO_2 reduction and dye degradation, Sol. Energ. Mat. Sol. C, 157 (2016) 406–414.

[8] F. Fresno, R. Portela, S. Suárez, J.M. Coronado, Photocatalytic materials: recent achievements and near future trends, J. Mater. Chem. A, 2 (2014) 2863–2884.

[9] J.C. Yu, L. Zhang, Z. Zheng, J. Zhao, Synthesis and characterization of phosphated mesoporous titanium dioxide with high photocatalytic activity, Chem. Mater., 15 (2003) 2280–2286.

[10] X. Wang, K. Maeda, A. Thomas, K. Takanabe, G. Xin, J.M. Carlsson, K. Domen, M. Antonietti, A metal-free polymeric photocatalyst for hydrogen production from water under visible light, Nat. Mater., 8 (2009) 76–82.

[11] Y. Zhang, Q. Zhang, Q. Shi, Z. Cai, Z. Yang, Acid-treated g-C_3N_4 with improved photocatalytic performance in the reduction of aqueous Cr(VI) under visible-light, Sep. Purif. Technol., 142 (2015) 251–257.

[12] S.C. Yan, Z.S. Li, Z.G. Zou, Photodegradation of Rhodamine B and Methyl Orange over B-doped g-C_3N_4 under visible light irradiation, Langmuir, 26 (2010) 3894–3901.

[13] N. Tian, H. Huang, Y. He, Y. Guo, Y. Zhang, Novel g-C_3N_4/$BiIO_4$ heterojunction photocatalysts: synthesis characterization and enhanced visible light-responsive photocatalytic activity, RSC. Adv., 4 (2014) 42716.

[14] Y. Wang, X. Wang, M. Antonietti, Polymeric graphitic carbon nitride as a heterogeneous organo catalyst: from photochemistry to multipurpose catalysis to sustainable chemistry, Angew. Chem. Int. Ed., 51 (2012) 68–89.

[15] J. Liu, Y. Zhang, L. Lu, G. Wu, W. Chen, Self-regenerated solar-driven photocatalytic water splitting by urea derived graphitic carbon nitride with platinum nanoparticles, Chem. Commun., 48 (2012) 8826–8828.

[16] T. Komatsu, Attempted chemical synthesis of graphite-like carbon nitride, J. Mater. Chem., 11 (2001) 799–801.

[17] Y.C. Zhao, D.L. Yu, O. Yanagisaw, K. Matsugi, Y.J. Tian, Structural evolution of turbostratic carbon nitride after being treated with a pulse discharge, Diam. Relat. Mater., 14 (2005) 1700–1704.

[18] H.A. Ma, X.P. Jia, L.X. Chen, P.W. Zhu, W.L. Guo, X.B. Guo, Y.D. Wang, S.Q. Li, G.T. Zou, G. Zhang, High-pressure pyrolysis study of $C_3N_6H_6$: a route to preparing bulk C_3N_4, J. Phys. Condens. Matter., 14 (2002) 11269.

[19] S.C. Yan, Z.S. Li, Z.G. Zou, Photo degradation performance of g-C_3N_4 fabricated by directly heating melamine, Langmuir, 25 (2009) 10397–10401.

[20] C. Zhou, C. Lai, D. Huang, G. Zeng, C. Zhang, M. Cheng, L. Hu, J. Wan, W. Xiong, M. Wen, X. Wen, L. Qin, Highly porous carbon nitride by supramolecular preassembly of monomers for photocatalytic removal of sulfamethazine under visible light driven, Appl. Catal. B: Environ., 220 (2018) 202–210.

[21] K.H. Leong, P.F. Lim, L.C. Sim, V. Punia, S. Pichiah, Improved solar light stimulated charge separation of g-C_3N_4 through self-altering acidic treatment, Appl. Surf. Sci., 430 (2018) 355–361.

[22] W.J. Ong, L.K. Putri, L.L.Tan, S.P. Chai, S.T. Yong, Hetero structured AgX/g-C_3N_4 (X = Cl and Br) nanocomposites via a sonication-assisted deposition-precipitation approach: Emerging role of halide ions in the synergistic photocatalytic reduction of carbon dioxide, Appl. Catal. B Environ., 180 (2016) 530–543.

[23] L.J. Fang, Y.H. Li, P.F. Liu, D.P. Wang, H.D. Zeng, X.L. Wang, H.G. Yang, Facile fabrication of large aspect ratio g-C_3N_4 nanosheets for enhanced photocatalytic hydrogen evolution, ACS. Sustainable. Chem. Eng., 5 (2017) 2039–2043.

[24] X. Chen, L. Zhang, B. Zhang, X. Guo, X. Mu, Highly selective hydrogenation of furfural to furfuruyl alcohol over Pt nanoparticles supported on g-C_3N_4 nanosheets catalysts in water, Sci. Rep., 6 (2016) 28558.

[25] L. Jiang, X. Yuan, G. Zeng, X. Chen, Z. Wu, J. Liang, J. Zhang, H. Wang, H. Wang, Phosphorus- and sulfur-codopedg-C_3N_4: facile preparation, mechanism insight, and application as efficient photocatalyst for tetracycline and methyl orange degradation under visible light irradiation, ACS Sustain. Chem. Eng., 5 (2017) 5831–5841.

[26] Y. Guo, T. Chen, Q. Liu, Z. Zhang, X. Fang, Insight into the enhanced photocatalytic activity of potassium and iodine Co doped graphitic carbon nitride photocatalysts, J. Phys. Chem. C, 120 (2016) 25328–25337.

[27] M. Jaysankar, W. Qiu, J. Bastos, J.G. Tait, M. Debucquoy, U.W. Paetzold, D. Cheyns, J. Poortmans, Crystallisation dynamics in wide-bandgap perovskite films, J. Chem. Mater. A, 4 (2016) 10524–10531.

[28] X.H. Li, J.S. Chen, X. Wang, J. Sun, M. Antonietti, Metal-free activation of dioxygen by graphene/g-C_3N_4 nanocomposites: functional dyads for selective oxidation of saturated hydrocarbons, J. Am. Chem. Soc., 133 (2011) 8074–8077.

[29] Y. Zhang, T. Mori, J. Ye, M. Antonietti, Phosphorus-doped carbon nitride solid: enhanced electrical conductivity and photocurrent generation, J. Am. Chem. Soc., 132 (2010) 6294–6295.

[30] J. Liu, Y. Liu, N. Liu, Y. Han, X. Zhang, H. Huang, Y. Lifshitz, S. T. Lee, J. Zho, Metal-free efficient photocatalyst for stable visible water splitting via a two-electron pathway, Science, 347 (2015) 970–974.

[31] J. Xu, F. Wu, Q. Jiang, Y.X. Li, Mesoporous carbon nitiride grafted with n-bromobutance: a highly performance heterogeneous catalyst for the solvent free cycloaddition of CO_2 to propylene carbonate, Catal. Sci. Technol., 5 (2015) 447–454.

[32] X. Du, G. Zou, X. Wang, Controllable and scalable synthesis of ordered mesoporous silica nanosheets by using acidified g-C_3N_4 as a lamellar, Nanotechnology, 28 (2017) 1–10.

[33] A. Shi, H.H. Li, S. Yin, B. Liu, J.C. Zhang, Y. Wang, Effect of conjugation degree and delocalized π-system on the photocatalytic activity of single layer g-C_3N_4, Appl. Catal. B Environ., 218 (2017) 137–146.

[34] C. Ronning, H. Feddermann, R. Mark, H. Hofsass, Carbon nitride deposited using energetic species: A review on XPS studies, Phys. Rev. B, 58 (1998) 2207–2215.

[35] B.R. Pistillo, K. Menguelti, D. Arl, F. Addiego, D. Lenoble, D. PRAP-CVD: how to design high conformal PEDOT surfaces, RSC Adv., 7 (2017) 19117–19123.

[36] J. Xiao, Y. Xie, H. Cao, Y. Wang, Z. Guo, Y. Chen, Towards effective design of active nanocarbon materials for integrating visible-light photocatalysis with ozonation, Carbon, 107 (2016) 658–666.

[37] W.J. Gammon, O. Kraft, A.C. Reilly, B.C. Holloway, Experimental comparison of N(1s) X-ray photoelectron spectroscopy binding energies of hard and elastic amorphous carbon nitride films with reference organic compounds, Carbon, 41 (2003) 1917–1923.

[38] T. Susi, T. Pichler, P. Ayala, X-ray photoelectron spectroscopy of graphitic carbon nanomaterials doped with heteroatoms, Beilstein J. Nanotech., 6 (2015) 177–192.

[39] F. Yang, V. Kuznietsov, M. Lublow, C. Merschjann, A. Steigert, J. Klaer, A. Thomas, T. Schedel-Niedrig, Solar hydrogen evolution using metal-free photocatalytic polymeric carbon nitride/$CuInS_2$ composites as photocathodes, J. Chem. Mater. A, 1 (2013) 6407–6415.

[40] L. Ge, F. Zuo, J. Liu, Q. Ma, C. Wang, D. Sun, L. Bartels, P. Feng, Synthesis and efficient visible light photocatalytic hydrogen evolution of polymeric g-c3n4 coupled with CdS quantum dots, J. Phys. Chem. C, 116 (2012) 13708–13714.
[41] F. Dong, Y. Li, Z.Y. Wang, W.K. Ho, Enhanced visible light photocatalytic activity and oxidation ability of porous graphene-like g-C_3N_4 nanosheets via thermal exfoliation, Appl. Surf. Sci., 358 (2015) 393–403
[42] M.J. McAllister, J.L. Li, D.H. Adamson, H.C. Schniepp, A.A. Abdala, J. Liu, M. Herrera-Alonso, D.L. Milius, R. Car, R.K. Prud'homme, I.A. Aksay, Single sheet functionalized graphene by oxidation and thermal expansion of graphite, Chem. Mater., 19 (2007) 4396–4404.
[43] W. Ho, J.C. Yu, J. Lin, J. Yu, P. Li, Preparation and photocatalytic behavior of MoS_2 and WS_2 Nanocluster Sensitized TiO_2, Langmuir, 20 (2004) 5865–5869.
[44] R. Zuo, G. Du, W. Zhang, L. Liu, Y. Liu, L. Mei, Z. Li, Photocatalytic degradation of Methylene Blue using TiO_2impregnated diatomite, Adv. Mater. Sci. Eng., (2014) 1–7.